

Optimized NiFe-based coordination polymer catalysts: Sulfur-tuning and *operando* monitoring of water oxidation

Yonggui Zhao,^{‡[a]} Wenchao Wan,^{‡[a]} Nanchen Dongfang,^[a] C. A. Triana,^[a] Lewis Douls,^[a] Chong Huang,^[a] Rolf Erni,^[b] Marcella Iannuzzi,^[a] and Greta R. Patzke*^[a]

^aDepartment of Chemistry, University of Zurich, Winterthurerstrasse 190, CH-8057 Zurich, Switzerland

E-mail: greta.patzke@chem.uzh.ch

^bElectron Microscopy Center, Empa, Swiss Federal Laboratories for Materials Science and Technology, Überlandstrasse 129, CH-8600 Dübendorf, Switzerland

*Corresponding author

[‡]These authors contributed equally

KEYWORDS *electrocatalysis, mechanisms, operando XAS, coordination polymers, oxygen evolution reaction*

ABSTRACT: In-depth insights into the structure-activity relationships and complex reaction mechanisms of oxygen evolution reaction (OER) electrocatalysts are indispensable to efficiently generate clean hydrogen through water electrolysis. We introduce a convenient and effective sulfur heteroatom tuning strategy to optimize the performance of active Ni and Fe centers embedded into coordination polymer (CP) catalysts. *Operando* monitoring then provided the mechanistic understanding as to how exactly our facile sulfur engineering of Ni/Fe-CPs optimizes the local electronic structure of their active centers to facilitate dioxygen formation. The high OER activity of our optimized S-R-NiFe-CPs outperforms most recent NiFe-based OER electrocatalysts. Specifically, we start from oxygen-deprived O_d-R-NiFe-CPs and transform them into highly active Ni/Fe-CPs with tailored sulfur coordination environments and anionic deficiencies. Our *operando* XAS analyses reveal that sulfur introduction into our designed S-R-NiFe-CPs facilitates the formation of crucial highly oxidized Ni⁴⁺ and Fe⁴⁺ species, which generate oxygen-bridged Ni^{IV}-O-Fe^{IV} moieties that act as the true OER active intermediates. The advantage of our sulfur-doping strategy for enhanced OER is evident from comparison with sulfur-free O_d-R-NiFe-CPs, where the formation of essential high-valent OER intermediates is hindered. Moreover, we proposed a dual-site mechanism pathway, which is backed up with a combination of pH-dependent performance data and DFT calculations. Computational results support the benefits of sulfur modulation, where a lower energy barrier enables O-O bond formation atop the S-Ni^{IV}-O-Fe^{IV}-O moieties. Our convenient anionic tuning strategy facilitates the formation of active oxygen-bridged metal motifs and can thus bring forward design of flexible and low-cost OER electrocatalysts.

The ongoing consumption of fossil fuels and the associated global environmental issues call for the general use of renewable energy resources.^{1,2} To date, water splitting is a promising strategy for sustainable energy conversion into green hydrogen as a flexible carrier and commodity.^{3,4} The overall efficiency of the water electrolysis process is mainly hindered by its sluggish oxygen evolution half-reaction (OER) that involves a demanding 4e⁻ transfer.⁵⁻⁷ Noble metal-based materials (e.g. Ru and Ir) still display the most promising OER performance, but their practical applications are limited by high costs and scarcity. However, the design of high-performance and low-cost OER electrocatalysts with earth-abundant elements remains challenging, and their targeted optimization requires fundamental mechanistic insights.

In the past decades, economic NiFe-based OER catalysts (e.g. alloys,⁸ carbides,⁹ coordination polymers,¹⁰ (oxy)hydroxides,¹¹ oxides,¹² sulfides,¹³ phosphides,¹⁴ and selenides¹⁵) attracted enormous interest due to their remarkable catalytic performance. However, fundamental questions concerning the nature of their catalytically active species and their intrinsic catalytic mechanisms are still intensely investigated. Several prerequisites for OER are now emerging: (1) The involvement of both Ni and Fe as catalytically active centers in a dual-site mechanism has meanwhile been proposed for various types of NiFe-based OER catalysts, such as NiFeO_x,¹⁶ FeCoCrNi alloy,¹⁷ and NiFe-based single-atom catalysts.¹⁸ (2) Increasing evidence has been garnered that both active sites are oxidized to high valent M(III/IV) states during the OER process.^{19,20} In the following, we now address the next questions to optimize NiFe-OER catalysts, starting from NiFe-coordination polymers: *How to facilitate (a) the formation of high valent states and then (b) their ability to form*

dual oxygen-bridged moieties with favorable energies for O-O bond formation?

Furthermore, the crucial role of engineered structural deficiencies and heteroatom incorporation in the formation of active sites and species remains to be investigated. Additionally, the precise structure-function relationships between modified/deficient local coordination environments and enhanced catalytic activity in related OER electrocatalysts need to be established. This will promote anionic modulation strategies for optimizing a wide range of OER materials. Both theoretical analyses and mechanistic studies of the real catalytically active intermediates are indispensable to resolve these long-standing challenges. We here apply density functional theory (DFT) in combination with time-resolved *operando* X-ray absorption spectroscopy (XAS) monitoring to capture the real catalytically active centers and their active intermediates.²¹⁻²⁴

We selected coordination polymers (CPs) as our target, because their virtually infinite options for connecting metal centers with organic or inorganic linkers attract considerable mechanistic and application-related research interest in many areas of catalysis.²⁵⁻²⁷ Their unique structural properties and high surface areas offer abundant accessible active sites for a wide range of catalytic reactions. These numerous active sites do not only improve the catalytic activity of CP-based electrocatalysts notably, but also provide more reliable signal-to-noise resolution during *operando* monitoring tests.²⁸⁻³¹

As for our structural tuning strategy, defect engineering has been identified as an effective strategy to optimize the OER performance of CP-based electrocatalysts for practical applications.^{10,26} Modulation of local coordination environments

through heteroatom incorporation is another promising approach to stabilize the structural deficiencies and to further optimize the catalytic activity.^{32,33} As mentioned above, the underlying structure-activity relationships remain to be explored and the stability of engineered structural deficiencies during long-time operations needs to be established.

Here, we introduce an anionic engineering strategy, starting from the sulfur-tuning of low-crystalline reduced NiFe-based CPs with a LDH-related structure that are rich in oxygen deficiencies (referred to as O_d-R-NiFe-CPs) as attractive template materials. Through the controlled introduction of sulfur heteroatoms, we first regulate the local coordination environments of the active centers and stabilize the oxygen deficiencies in the generated S-R-NiFe-CPs. Further, we combine computational modeling with manifold characterizations (*e.g.* XAS, electron paramagnetic resonance (EPR), and X-ray photoelectron spectroscopy (XPS)) to compare the local metal coordination environments of O_d-R-NiFe-CPs and S-R-NiFe-CPs. Interestingly, our results from structural characterizations show that sulfur atoms rather refill the oxygen deficiencies around Ni sites than substitute the oxygen centers.

Importantly, engineered S-R-NiFe-CPs were found to show superior OER electrocatalyst performance with a much lower overpotential of 245 mV at 20 mA/cm² and a very smaller Tafel slope value of 30.28 mV/dec over the pristine O_d-R-NiFe-CPs (271 mV and 49.10 mV/dec). Moreover, S-R-NiFe-CPs also outperformed most state-of-the-art NiFe-based electrocatalysts.

Operando XAS tests and DFT simulations unraveled the productive influence of sulfur heteroatom engineering on the regulation of local coordination environments and the resulting optimization of OER pathways. Our combined theoretical and experimental evidence demonstrates that targeted incorporation of S atoms into the oxygen-deficient NiFe-CP matrix clearly opti-

mizes the intrinsic OER mechanism. Controlled partial incorporation of S atoms notably facilitates the formation of true active Ni^{IV}-O-Fe^{IV} intermediate moieties in S-R-NiFe-CPs during the OER when compared to sulfur-free O_d-R-NiFe-CPs. These true active intermediates enable a dual-site mechanism (DSM) pathway *via* O-O bond formation atop the Ni^{IV}-O-Fe^{IV} moieties, giving rise to the observed high catalytic performance.

RESULTS AND DISCUSSION

Theoretical insights into the local coordination environments

DFT calculations can offer direct guidance for identifying the local coordination environments of Ni/Fe centers in O_d-R-NiFe-CPs after incorporation of S atoms. To the best of our knowledge, the sulfidation reaction can in principle proceed *via* the following four possible reaction pathways (**Figure S1**): i) S atoms refill the oxygen-deficient sites to form model structure **S1**; ii) model structure **S2** is constructed by substitution of the neighboring O atoms with S atoms near the deficiency site; iii) S atoms replace the shared O atoms from the di-μ-oxo Ni-Fe and Ni-Ni moieties in model structure **S3**; iv) model structure **S4** is formed *via* substitution of the shared O atoms from two di-μ-oxo Ni-Ni moieties with S atoms. As demonstrated in **Figure 1a**, our DFT calculations reveal that the proposed model structure **S1** shows the lowest formation energy, thus representing the most stable structural motif. We further calculated the differential electron density to explore the role of S atom modification in the charge distributions with the proposed model structures. As shown in **Figure 1b**, the proposed models of **S1-S4** exhibit intense charge distributions of metal centers nearby the S atoms. These charge distributions are crucial for tuning the adsorption properties of OER intermediates and for promoting the sluggish OER kinetics.^{7,34,35} This is also supported by the calculated projected density of states (PDOS) (**Figure 1c**), in

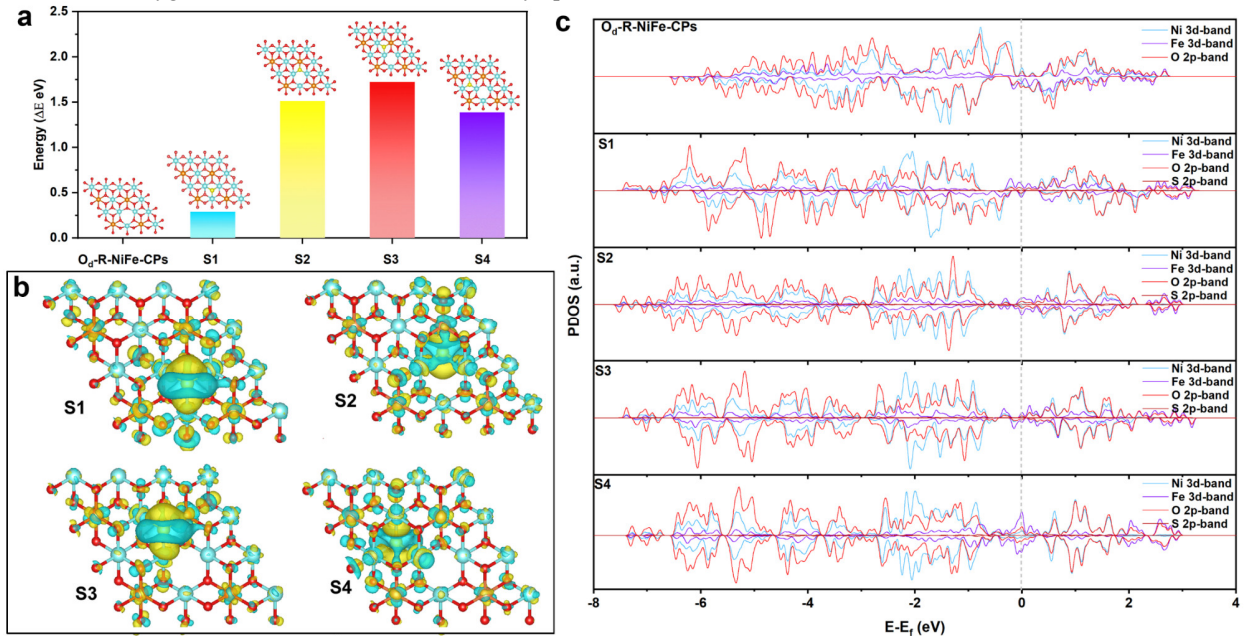


Figure 1 (a) Comparison of the calculated energy of proposed model structures with O_d-R-NiFe-CPs as a reference. (b) Differential charge density plots for proposed model structures of S1~S4 (cyan = electron depletion, yellow = electron accumulation). (c) Simulated projected density of states (PDOS) of O_d-R-NiFe-CPs, S1, S2, S3, and S4 model structures.

which the different proposed models with S atom incorporation show different electronic structures near the Fermi level. Specifically, the metal d-band states of **S1-S4** models shifted away from the Fermi level compared with the pristine model, demonstrating the weakened bond strength between metal and oxygen.^{2,10,22} This indicates that the incorporation of S heteroatoms can promote the desorption of OER intermediates (e.g. OO^* and HOO^*). As a result, the OER activity of O_d -R-NiFe-CP can be optimized *via* the incorporation of heteroatom S.

Synthesis and characterization of O_d -R-NiFe-CPs and S-R-NiFe-CPs

In light of the above DFT investigations, we designed the following experiments. First, O_d -R-NiFe-CPs were prepared according to our previous work with slight modifications.¹⁰ S-R-NiFe-CPs samples with different starting amounts of S for heteroatom modification (2, 5, 10, 20, and 50 mg) were prepared using a similar reduction and hydrothermal reaction strategy to that applied for O_d -R-NiFe-CPs. (see experimental methods, **Figures S2-S14**, and details in Supplementary Discussion I). (Note: the atomic Ni/Fe ratio of O_d -R-NiFe-CPs was determined as 3.51:1 based on ICP-MS results in **Table S2**. S-modified samples are referred to as S-R-NiFe-CPs in the following. If not otherwise mentioned, S-R-NiFe-CPs specifically refers to the optimized sample with the incorporation of 5 mg of thioacetamide (TAA) with an Ni/Fe/S atomic ratio of 3.58:1:0.79 (**Table S2**)). The results indicate that the incorporation of low S amounts (2 and 5 mg) does not affect the pristine crystal structure of O_d -R-NiFe-CPs. Moreover, the incorporated S atoms favorably enter the lattice of O_d -R-NiFe-CPs forming the proposed model structure **S1**, as illustrated in **Figure 1** and **Figure S1**. When a high amount of S atoms (> 10 mg) was introduced, some S atoms can still partially enter the lattice of O_d -R-NiFe-CPs based on the proposed reaction pathway **S1**. However, the excess S atoms are assumed to further activate the reaction pathway **S4**, giving rise to the formation of a secondary phase in S-R-NiFe-CPs (10 ~ 50 mg) (**Figures S5-S8**).

The influence of the synthetic preparation parameters, such as time and reaction temperature of the sulfidation process, on the structural and morphological properties of S-R-NiFe-CPs was also investigated (**Figures S9-S13**). These results revealed that the aforementioned two preparative parameters exhibited negligible influences on the structural and morphological properties of the final products. Furthermore, NiFe-based oxides (NiFe-O) and their reference samples with S modification (S-NiFe-O) were synthesized for further comparison (see experimental details and methods in the Supplementary Information and **Figures S15-S17**). The obtained results corroborate that partial substitution of O by S in NiFe-O can be performed while preserving its pristine high-crystallinity and rock salt-type crystal structure.

Ex situ XAS characterization

To elucidate the local electronic structure and coordination environment of Ni/Fe centers in as-prepared O_d -R-NiFe-CPs and S-R-NiFe-CPs, we performed X-ray absorption spectroscopy (XAS) tests at the Ni and Fe K-edge. As evident from Ni K-edge X-ray absorption near edge structure (XANES) spectra (**Figure 2a**), the rising absorption edge positions of O_d -R-NiFe-CPs, S-R-NiFe-CPs, NiFe-O, and S-NiFe-O are very close to those of

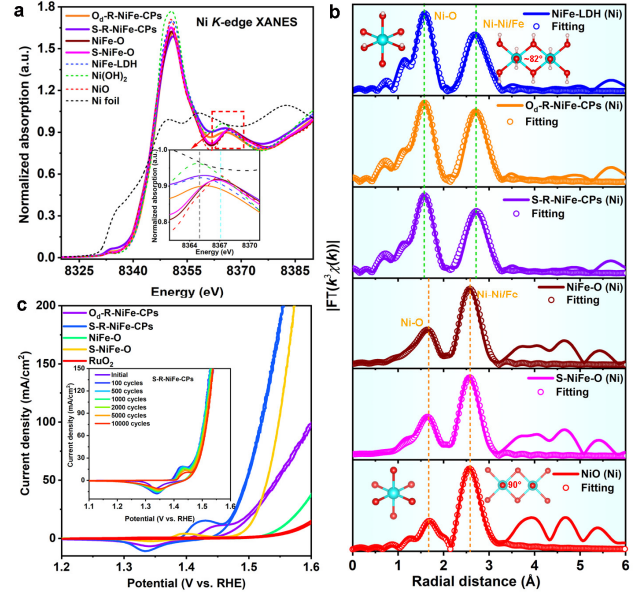


Figure 2 (a) Ni K-edge XANES spectra of the as-prepared samples vs. references. (b) Fitting of the Ni K-edge FT-EXAFS spectra of the as-prepared samples vs. references. (c) CV curves of as-prepared catalysts vs. reference RuO_2 with 90%-iR corrections (the inset represents CV cycling measurements).

the reference samples NiO, Ni(OH)_2 , and NiFe-LDH. This indicates that the average valence state of Ni ions in the as-synthesized samples are predominantly Ni^{2+} . A close inspection of the Ni K-edge XANES spectra illustrates that O_d -R-NiFe-CPs and S-R-NiFe-CPs exhibit similar spectral features at ~ 8365 eV (inset in **Figure 2a**), which originate from dipolar electronic transitions from Ni 1s to Ni/Fe 4p orbitals.³⁶⁻³⁸ A similar phenomenon was also observed in NiFe-O, S-NiFe-O, and reference NiO, which feature a similar peak at ~ 8367 eV.

The Ni K-edge extended X-ray absorption fine structure (EXAFS) spectra were further recorded to investigate the local coordination environment of Ni ions in the as-prepared materials. As shown in **Figure S18**, O_d -R-NiFe-CPs, S-R-NiFe-CPs, and reference NiFe-LDH display almost identical Ni K-edge EXAFS oscillations, indicating their similar local Ni environments, in line with the above analyses of XANES spectra (**Figure 2a**). Comparison of EXAFS spectra of NiFe-O, S-NiFe-O, and reference NiO indicates similar local coordination environments of their Ni centers. Fitting of the Fourier-transform (FT) EXAFS spectra, as shown in **Figure 2b**, indicates that all the investigated samples display two main backscattering peaks within the interval $R+\Delta R = 1\sim 3$ Å. The first backscattering peak in the FT-EXAFS spectra is attributed to the first coordination shells of Ni-O pairs. The second one is ascribed to the backscattering of the second coordination shells of Ni-Ni/Fe pairs. The first and second backscattering peaks in the FT-EXAFS spectra of NiO analogs are located at slightly different $R+\Delta R$ values compared with those of NiFe-LDH analogs. This is mainly attributed to their local structural differences (structural scheme as shown in **Figure 2b**). Fitting results for the FT-EXAFS spectra of O_d -R-NiFe-CPs (**Figure 2b** and **Table S3**) provided coordination numbers for Ni-O bonds ($\text{CN}_{\text{Ni-O}}$) and $\text{CN}_{\text{Ni-Ni/Fe}}$ of 5.15 and 6.00, respectively. The slightly lower $\text{CN}_{\text{Ni-O}}$ value of 5.15 calculated for O_d -R-NiFe-CPs compared with that of NiFe-LDH ($\text{CN}_{\text{Ni-O}}:6.00$) indicates that the as-prepared O_d -R-NiFe-

CPs are rich in oxygen deficiencies. Fitting of the FT-EXAFS spectra of S-R-NiFe-CPs provided CN_{Ni-O} and $CN_{Ni-Ni/Fe}$ values of 5.11 and 6.00, respectively. Moreover, the CN_{Ni-S} value was calculated as 0.32 in S-R-NiFe-CPs, suggesting that S atoms predominantly refill the oxygen deficiencies.

The Fe K-edge XAS data suggest similar coordination environments for the Fe centers among the investigated samples (**Figure S19 and Table S4**), which further supports that the sulfidation reaction follows the proposed reaction pathway **S1** (**Figure S1**). Analysis of the XAS data (**Figures S20-S23**) of S-R-NiFe-CPs (2 ~ 50 mg) suggests that the oxygen deficiencies around the Ni sites are first refilled by S atoms after the sulfidation reaction with a low amount of S atoms. However, with a higher amount of S atoms, the additional sulfur atoms can further partially replace O atoms around Ni sites leading to obvious structural changes. For comparison, the local coordination environments of Ni/Fe centers of NiFe-O and S-NiFe-O were investigated as well based on the respective EXAFS and FT-EXAFS spectra (**Figure 2b, Figures S18, S19b,c and Tables S3, S4**). The results indicate that the reference oxide samples with the absence of structural deficiencies followed the proposed reaction pathway **S4** during the sulfidation process. This is consistent with the above XAS studies of S-R-NiFe-CPs with a high amount of TAA (50 mg).

To further explore the role of S atom incorporation into the oxygen-deficient sites and in the surface chemical compositions, electron paramagnetic resonance (EPR) and X-ray photoelectron spectroscopy (XPS) analyses were carried out with the as-prepared samples. As expected, the results obtained from EPR and XPS analyses (**discussions and details in Figures S24-S26**) are in agreement with the above XAS analyses. These results in their entirety confirm that the incorporation of S heteroatoms likely refills the oxygen-deficient sites first. An excess amount of S atoms can activate the partial exchange reaction between the introduced S heteroatoms and oxygen atoms coordinated to the Ni sites.

Operando XAS characterization of S-R-NiFe-CPs towards OER

The electrochemical characterization reveals the superior OER activity of S-R-NiFe-CPs compared to that of O_d -S-R-NiFe-CPs (**Figure 2c and Figures S27-S36 and details in Supplementary Discussion II**). To identify the intrinsic structure-activity relationships and to understand the complex catalytic mechanism during OER, we performed *operando* XAS tests with the investigated catalysts in 0.1 M KOH (see **experimental details and methods in the Supplementary Information and in Figure 3 and Figures S37-S41**).

Operando XANES spectra (Ni K-edge): As shown in **Figure 3a**, for the *operando* Ni K-edge XANES spectra of S-R-NiFe-CPs recorded at the applied potentials from 0.8 V to 1.45 V vs. RHE, the rising absorption edges display a positive shift towards higher energy, reflecting the oxidation of Ni ions. **Figure 3b** shows the correlation between the rising absorption edge positions and the average valence states of Ni ions. The nominal valence states of Ni ions in our study were determined based on the reference samples β -NiOOH (8343.70 eV with Ni^{3+})³⁹⁻⁴¹ and γ -NiOOH (8345.00 eV with $Ni^{3.6+}$).³⁹⁻⁴¹ A close inspection of the variations of the valence state of Ni ions reveals three different reaction processes within the applied potential ranges. At

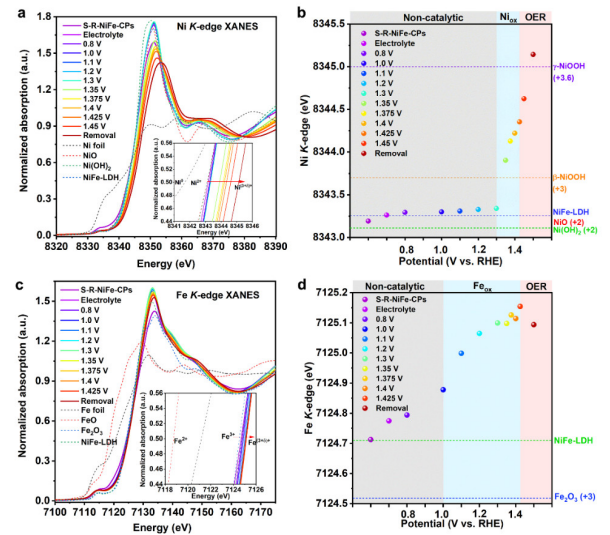


Figure 3 (a, c) *Operando* Ni and Fe K-edge XANES spectra of S-R-NiFe-CPs at different anodic potentials in 0.1 M KOH for OER. (b, d) Ni and Fe K-edge positions vs. applied potentials (Ni_{ox} and Fe_{ox} represent the oxidations of Ni and Fe, respectively. The Ni K-edge positions of γ -NiOOH and β -NiOOH are reported from references 39-41). (Note: when the applied potentials were higher than 1.45 V at the Ni K-edge and 1.425 V vs. RHE at Fe K-edge, respectively, the formation of oxygen bubbles drastically influences the quality of Ni and Fe K-edge XAS signals (**Figure S39**). Therefore, we only show the Ni and Fe K-edge XAS data below the mentioned potentials.)

non-catalytic potentials (0.8 to 1.3 V vs. RHE), the valence state of Ni ions mainly corresponds to Ni^{2+} . Meanwhile, a slight increase in the valence state of Ni ions is observed, which is mainly due to the chemisorption of OH^- from the electrolyte.^{42,43} When the applied potentials were increased from 1.3 to 1.425 V vs. RHE, the energy shifts of the rising absorption edge positions are ascribed to the oxidation of Ni ions (denoted as Ni_{ox}). In the Ni_{ox} region, the valence state of Ni ions shows an obvious increasing trend. With a further increase of the anodic potentials above 1.425 V vs. RHE, OER sets in along with the formation of high-valence Ni ions (**Figure 3b**). Previous *operando* studies have demonstrated that the high valence states of active metal centers generally recover to a lower value after removing the applied potentials.⁴⁴⁻⁴⁶ However, in our case (**Figure 3b**), an abnormal maximum value of valence state of Ni ions with a rising absorption edge position of 8345.14 eV, which is even higher than reference γ -NiOOH (8345.00 eV), is observed after the removal of the applied potentials. In fact, the applied potentials were set in the range of 0.8 to 1.5 V vs. RHE in the investigated catalysts during the *operando* tests, which are higher than the aforementioned potentials (0.8 to 1.45 V vs. RHE) in **Figure 3b**. When the applied potentials were higher than 1.45 V vs. RHE, the Ni K-edge XAS signals were drastically distorted by the generation of O_2 bubbles (**Figure S39a**). Therefore, we only show the Ni K-edge XAS data below 1.45 V vs. RHE in **Figure 3b**. Given the increased valence states of Ni ions in the samples after removing the potentials compared with those present at 1.45 V vs. RHE, we propose that the main active Ni species during the OER originate from the formation of high-valent Ni^{4+} species. This is in line with recent *operando* studies on Ni-based OER electrocatalysts.⁴⁷⁻⁴⁹

Operando XANES spectra (Fe K-edge): The energy shifts in the rising absorption edge position of Fe K-edge XANES spectra and the changes in the valence states of Fe ions show slight differences compared with those of the Ni K-edge (Figure 3c,d): i) The non-catalytic region was defined for potentials below 1.0 V vs. RHE, ii) the oxidation of Fe (denoted as Fe_{ox}) occurred in the range from 1.0 to 1.425 V vs. RHE, iii) OER was activated along with the formation of Fe^{(3+σ)⁺} (0 < σ < 1) species above 1.425 V vs. RHE, iv) after the removal of the applied potentials, the valence states of Fe ions slightly recovered to a lower value (Figure S39b). Compared with the analyses of the Ni K-edge XANES spectra (Figure 3a,b), the Fe K-edge XANES spectra indicate an earlier trigger potential of the Fe_{ox} region suggesting that the Fe sites undergo an early deprotonation process (OH⁻ → O* + H⁺ + e⁻).^{50,51} In summary, investigations of the Ni and Fe K-edge XANES spectra of S-R-NiFe-CPs demonstrate that both Ni and Fe centers undergo oxidation to form high-valent species (Ni^{(3+σ)⁺} and Fe^{(3+σ)⁺}), suggesting that they both play a pivotal role during the OER process.^{12,42,52,53}

Operando monitoring of the dynamics of the local coordination environments during the OER

Operando EXAFS spectra (Ni K-edge): The dynamics of the local coordination environments of Ni centers in S-R-NiFe-CPs towards OER were further evaluated from *operando* FT-EXAFS spectra (Figure 4). For Ni K-edge FT-EXAFS spectra of S-R-NiFe-CPs immersed into the electrolyte (Figure 4a), two apparent peaks are observed with radial distances R+ΔR of 1.59 Å and 2.70 Å, arising from the backscattering of Ni^{II}-O/S and Ni^{II}-Ni^{II}/Fe^{III} pairs, respectively. In the non-catalytic region (0.8 to 1.3 V vs. RHE), these two scattering peaks remain unchanged. This can be further confirmed by the fitting of EXAFS spectra, in which both the interatomic distances and the coordination numbers of Ni^{II}-O/S and Ni^{II}-Ni^{II}/Fe^{III} pairs exhibit negligible changes (Figure 4a and Table S5). Similar observations are also evident from the WT-EXAFS spectra. As shown in Figure 4a, for the samples immersed into the electrolyte and with an applied potential of 1.3 V vs. RHE, the scattering signals of

Ni^{II}-O/S and Ni^{II}-Ni^{II}/Fe^{III} pairs exhibit similar intensities. When the applied potentials are higher than 1.3 V vs. RHE, the FT-EXAFS spectra (Figure 4a) of S-R-NiFe-CPs feature an additional scattering peak with a radial distance R+ΔR = 2.39 Å, indicating the formation of disordered Ni^{III}-O-Ni^{III}/Fe^{III} moieties. Furthermore, with an increase of the anodic potentials, this newly formed scattering peak displays changes in its profile, indicating the oxidation of Ni²⁺ to Ni^{3+/4+}. The WT-EXAFS spectra further support the results derived from the FT-EXAFS spectra. As shown in Figure 4b, the scattering peaks of Ni^{II}-Ni^{II}/Fe^{III} pairs splits into two separate scattering signals at 1.35 V vs. RHE. The newly formed scattering signal indicating a shorter interatomic distance that is ascribed to the formation of Ni^{III}-Ni^{III}/Fe^{III} pairs. Then, these scattering pairs underwent further peak profile changes and reached their maximum intensity after the removal of the potentials. Moreover, during the anodic polarization, the Ni K-edge FT-EXAFS spectra of S-R-NiFe-CPs (Figure 4a) also reveal a negative peak shift of Ni^{II}-O/S pairs, illustrating oxidation process from Ni^{II}-O/S to Ni^{III}-O/S. For the FT-EXAFS spectra above 1.425 V vs. RHE, a weakened scattering peak at a radial distance R+ΔR = 1.87 Å is present, which is distinct from the scattering peak with stronger intensity arising from an interatomic distance of 1.47 Å. When we combine the above observations with the variations in the valence state of Ni ions in Figure 4b, we can conclude that the appearance of the stronger scattering peak at 1.47 Å arises from the formation of Ni^{III/IV}-O coordination shells. The scattering peak with weakened intensity at 1.87 Å is ascribed to the preserved backscattering of the Ni-S coordination shell. This conclusion is also supported by the Ni K-edge WT-EXAFS spectra (Figure 4b), where a scattering peak with a weakened signal emerges at 1.87 Å above 1.425 V vs. RHE. As expected, the fitting results of the *operando* Ni K-edge FT-EXAFS spectra (Table S5) show an increased CN value of Ni^{III}-O and Ni^{III}-Ni^{III}/Fe^{III} pairs during the *operando* OER experiment. In contrast, the CN values of Ni^{II}-O and Ni^{II}-Ni^{II}/Fe^{III} exhibit a decreasing trend. The CN values of Ni-S pairs remain quite unchanged, which indicates the structural stability of S-Ni-O-Fe-O moieties during the OER process.

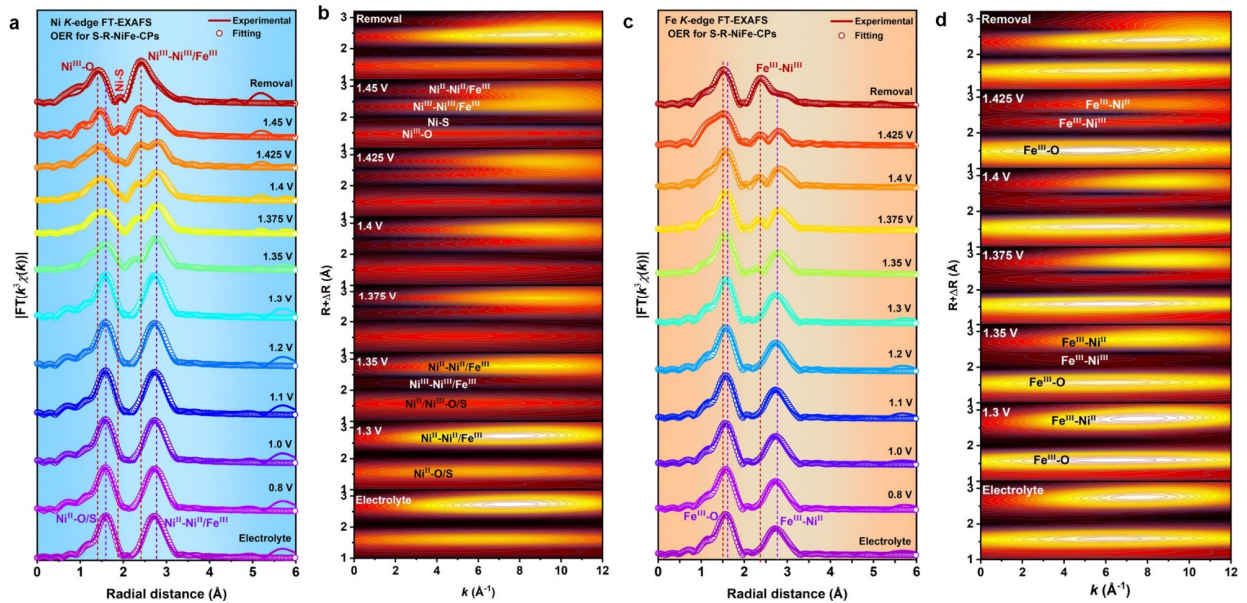


Figure 4 (a, c) Fitting of *operando* Ni and Fe K-edge FT-EXAFS of S-R-NiFe-CPs at different anodic potentials in 0.1 M KOH for OER. (b, d) Ni and Fe K-edge WT-contour plots of S-R-NiFe-CPs recorded at anodic potentials in 0.1 M KOH for OER.

Operando EXAFS spectra (Fe K-edge): The *operando* Fe K-edge FT-EXAFS spectra (Figure 4c,d) show similar peak shape alterations in the second coordination shells compared with the Ni K-edge (Figure 4a,b). Due to the quite low Fe to Ni ratio in S-R-NiFe-CPs (Tables S2), it is reasonable to propose that the observed signal changes from the second coordination shells arise from the oxidative transformation of $\text{Fe}^{\text{III}}\text{-O-Ni}^{\text{II}}$ into $\text{Fe}^{\text{III}}\text{-O-Ni}^{\text{III}}$ configurations. As indicated in Figure 4c and Tables S6, during anodic polarization, the average interatomic distances starting from $\text{Fe}^{\text{III}}\text{-O}$ decrease slightly, suggesting the oxidation of Fe^{3+} to Fe^{4+} . This is also largely in agreement with the analyses of the Fe K-edge XANES spectra (Figure 3c,d). Interestingly, neither the FT-EXAFS nor the WT-EXAFS spectra show any extra scattering peaks in the first coordination shell besides the formation of $\text{Fe}^{\text{III/IV}}\text{-O}$. This further implies that the introduced S atoms mainly refill the oxygen deficiencies around the Ni sites (Figure S1).

Combination of *operando* XANES and FT-EXAFS investigations unambiguously reveals that the *in situ* formed oxygen-bridged $\text{S-Ni}^{\text{IV}}\text{-O-Fe}^{\text{IV}}\text{-O}$ moieties with the high-valent $\text{Ni}^{(3+\sigma)+}$ and $\text{Fe}^{(3+\sigma)+}$ species are prerequisites to initiate OER in S-R-NiFe-CPs. In other words, these high-valent structural moieties are serving as the true active species during the OER.

Influence of sulfur modification on the OER: To understand the role of S atom modification in the OER catalytic activity, *operando* XAS tests on $\text{O}_d\text{-R-NiFe-CPs}$ for OER were further performed in 0.1 M KOH. Our results (Figures S40-S41) evidence that the formation of $\text{Ni}^{\text{III/IV}}\text{-O-Fe}^{\text{III/IV}}$ configurations in $\text{O}_d\text{-R-NiFe-CPs}$ is hindered when compared with S-R-NiFe-CPs. It should be emphasized that our experimental results corroborate the formation of Fe^{4+} species in both $\text{O}_d\text{-R-NiFe-CPs}$ and S-R-NiFe-CPs for OER (Figure 3c,d and Figure S41a,b). Such evidence can reflect that the as-investigated catalysts proceed via a similar OER catalytic mechanism at the Fe sites. However, this does not infer that only Fe centers act as the catalytically active sites but rather reflects that the deprotonation process ($\text{OH}^- \rightarrow \text{O}^* + \text{H}^+ + \text{e}^-$) preferably proceeds on Fe sites rather than on Ni sites. This can also indicate that Fe sites are not rate-determining for the OER process in contrast to Ni sites.^{47,54,55}

We further conducted *operando* EIS tests to explore the interface behavior between the as-prepared catalysts and electrolytes. The *operando* EIS investigations (discussions and details in Figure S42) in their entirety corroborate that the oxidation of Ni in $\text{O}_d\text{-R-NiFe-CPs}$ is promoted with partial S atom introduction. This is also in agreement with the observations from our previous *operando* XAS analyses (Figure 3).

DFT simulations

To gain insight into the origins of the OER activity and to decipher the underlying reaction pathways, DFT simulations were carried out using structural models of the investigated catalysts. As supported by our *operando* XAS results (Figures 3 and 4 and Figures S37-S41), both Ni and Fe ions in S-R-NiFe-CPs underwent oxidation into high-valent species (Ni^{4+} and Fe^{4+}), suggesting that they are all involved in the OER process. This can also indicate that the *in situ* formed $\text{Ni}^{\text{IV}}\text{-O-Fe}^{\text{IV}}$ moieties act as the real active sites and account for the excellent OER activity of S-R-NiFe-CPs. The investigation of pH-dependent OER activity of the investigated catalysts can provide further evidence to recognize the real active sites and to understand the catalytic OER mechanisms.^{7,16,42,56,57} As shown in Figure S43, it is apparent that both $\text{O}_d\text{-R-NiFe-CPs}$ and S-R-NiFe-CPs exhibit enhanced OER activity from a pH value of 12.82 to 14.00. Moreover, both investigated catalysts show a super-Nernstian behavior, indicating that the as-investigated catalysts undergo a decoupled proton-electron transfer (PT/ET) pathway. Previous studies indicated that the appearance of the PT/ET pathway is strong evidence for the presence of a dual-site reaction mechanism (DSM).^{16,42,56-59}

According to the attained information, DFT calculations based on the proposed DSM were carried out for our catalysts (see experimental details in the Supporting Information). For comparison, DFT calculations of the conventional adsorbate evolution mechanism (AEM) were also performed (Figure S44). It should be noted that the OER intermediates via an AEM pathway can be adsorbed either on the Ni sites or on the Fe sites. Therefore, we calculated the Gibbs free energies of OER intermediates adsorbed on the individual Ni and Fe sites in $\text{O}_d\text{-R-NiFe-CPs}$.

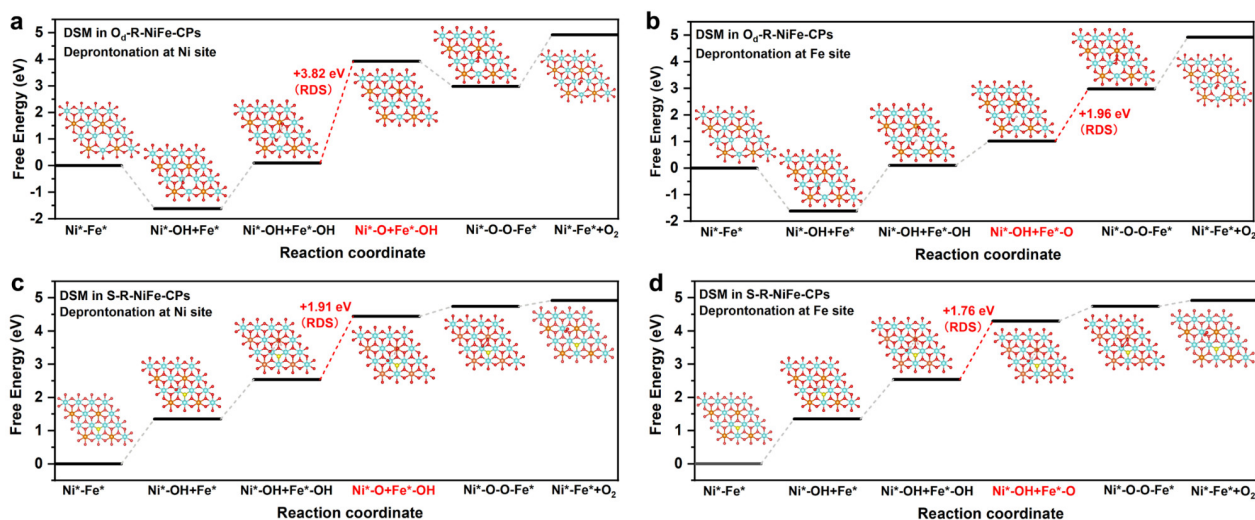


Figure 5 (a, b) Calculated free energy diagrams of OER intermediates adsorbed on $\text{O}_d\text{-R-NiFe-CPs}$ via DSM. (c, d) Calculated free energy diagrams of OER intermediates adsorbed on S-R-NiFe-CPs via DSM.

NiFe-CPs, respectively. The AEM results (**discussions and details in Figure S44**) suggest that the Fe sites in O_d-R-NiFe-CPs are thermodynamically more active compared with Ni sites during the OER process. However, as this is not consistent with our previous *operando* XAS analyses and pH-dependent experiments (**Figures 3 and 4 and Figures S37-S41, S43**), the conventional AEM might not be the right model to describe our catalysts.

We thus focused on the DSM pathway for the as-investigated catalysts. It should be emphasized that the deprotonation process of M^{*}-OH can follow two possible pathways in the proposed DSM: i) the deprotonation occurs at the Ni site to generate Ni^{*}-O+Fe^{*}-OH intermediates (**Figure 5a,c**), ii) the Fe sites serve as the target sites for the deprotonation process (**Figure 5b,d**), thereafter, forming Fe^{*}-O+Ni^{*}-OH intermediates. For the investigated O_d-R-NiFe-CPs model, our computational results (**Figure 5a,b and Figure S45**) unravel a lower energy barrier for the deprotonation of M^{*}-OH at the Fe sites in contrast to the Ni sites, suggesting that the Fe sites are more favorable for the deprotonation of M^{*}-OH. This is also in agreement with our above-mentioned *operando* XAS results (**Figures 3 and 4**). The rate-limiting step (RLS) of DSM in O_d-R-NiFe-CPs is identified as the O-O bond formation atop of Ni-O-Fe moiety showing a very low energy barrier of 1.96 eV, more convenient than for the AEM pathway (2.51 eV at Ni site and 2.27 eV at Fe site). This indicates that the OER in O_d-R-NiFe-CPs is thermodynamically more favorable *via* a DSM pathway.

We further calculated the free energy diagram of OER steps in S-R-NiFe-CPs based on the proposed DSM. As shown in **Figure 5c,d and Figure S46**, our calculations imply that the formation of O^{*} atop of Ni-O-Fe sites with an energy barrier of 1.76 eV in the S-R-NiFe-CP model is the RLS, which is lower in energy than for the O_d-R-NiFe-CPs model system. Moreover, the as-prepared S-R-NiFe-CPs only need a very low energy barrier of 0.44 eV to activate the formation of O-O bond atop of Ni-O-Fe sites (**Figure 5d**), better than the O_d-R-NiFe-CPs (1.96 eV) (**Figure 5b**). Such a lower energy barrier corroborates the superior OER performance of S-R-NiFe-CPs, in line with our experimental electrochemical results (**Figure 2c**). This unambiguously demonstrates the benefits of engineering the contents of S centers to improve the OER activity of O_d-R-NiFe-CPs catalysts.

Combining our DFT simulations with our experimental evidence, **Figures S45-S46** illustrate the overall schematic OER pathway (DSM) for the as-investigated O_d-R-NiFe-CP and S-R-NiFe-CP catalysts. Based on our investigations, targeted S atom modification plays a pivotal role in the optimization of the local electronic structure and adsorption behavior of the OER intermediates in S-R-NiFe-CPs. As a benefit of this strategy, high-valent Ni⁴⁺ and Fe⁴⁺ species are favorably formed in S-R-NiFe-CPs (**Figure 3**), which can induce an enhanced concentration of holes in the oxidized oxygen intermediates.^{60,61} These oxygen intermediates can be further activated by the facilitated formation of Ni^{IV}-O-Fe^{IV} moieties which further promote the generation of O₂. As a result, the as-prepared S-R-NiFe-CP catalysts excel through superior OER activity.

CONCLUSIONS

We introduce a convenient and economic anionic engineering strategy to design highly efficient S-R-NiFe-CP OER electrocatalysts from reduced coordination polymers that outperform most reported NiFe-based catalysts. This strategy promotes the formation of crucial high-valent OER intermediates and their subsequent O-O bond formation, as demonstrated with complementary theoretical and *in situ* experimental investigations.

Controlled sulfur introduction preferably refills the oxygen deficiencies around Ni sites in the rationally constructed S-R-NiFe-CPs. Tuned sulfur contents thus regulate the electronic structure and optimize the local coordination environments of the active centers in S-R-NiFe-CPs. *Operando* XAS studies showed that sulfur engineering facilitates the formation of high-valent Ni⁴⁺ and Fe⁴⁺ species in S-R-NiFe-CPs, followed by their convenient reconstruction into S-Ni^{IV}-O-Fe^{IV}-O moieties during the OER process. In contrast, analogous OER *operando* XAS tests of sulfur-free O_d-R-NiFe-CPs revealed that the formation of key Ni^{III/IV}-O-Fe^{III/IV} units was hindered. This is clear evidence for the beneficial influence of sulfur anionic tuning on the formation of key OER intermediates.

pH-dependent investigations of both catalyst types further elucidated their intrinsic OER mechanisms. Our results reveal a super-Nernstian behavior with decoupled proton-electron transfer (PT/ET) characteristics for both O_d-R-NiFe-CP and S-R-NiFe-CP catalysts, suggesting that their OER processes proceed *via* a dual-site mechanism (DSM) pathway. DFT simulations further highlight the crucial role of S atoms in tuning the free energy of the individual OER steps for the CP catalysts. Due to their optimized adsorption behavior for OER intermediates, the as-prepared S-R-NiFe-CPs accelerate the reaction kinetics and exhibit a high OER activity that outperforms most recently reported NiFe-based OER electrocatalysts.

Our anionic modulation strategy for the heteroatom-driven engineering of OER mechanisms guide the rational design of low-cost water splitting electrocatalysts through convenient structural tuning of their sublattices and defects. We expect our comprehensive and mechanism-driven approach to optimize the activity of a wide range of coordination polymers and heterogeneous catalysts.

EXPERIMENTAL METHODS

Chemicals. Nickel(II) chloride (≥ 98 %), nickel(II) nitrate hexahydrate (≥ 99.999 %), iron(II) chloride tetrahydrate (≥ 99 %), potassium tetracyanonickelate(II) hydrate (≥ 99 %), potassium hydroxide (≥ 99.97 %), sodium borohydride (≥ 98 %), trisodium citrate dihydrate (≥ 99 %), and thioacetamide (≥ 99 %) were purchased from Sigma-Aldrich. All chemicals were used as received without any further purification.

Synthesis of NiFe-based coordination polymers (NiFe-CPs). NiFe-CPs were prepared based on our previous study with slight modifications.¹⁰ In a typical synthetic procedure, 1.6 mmol of nickel(II) chloride, 0.4 mmol of iron(II) chloride tetrahydrate, and 1.5 mmol of trisodium citrate dihydrate were dissolved into 100 mL of deionized (DI) water and stirred for 15 min (denoted as solution A). Meanwhile, 2 mmol of potassium tetracyanonickelate(II) was dissolved into 100 mL of DI water and stirred for 15 min (denoted as solution B). Then, solution B was rapidly injected into solution A under magnetic stirring for 3 min. The solution mixture was aged for another 24 h at room temperature. Afterward, the as-obtained precipitations were collected by centrifugation and washed with

ethanol and water several times. Finally, the collected samples (NiFe-CPs) were transferred into a drying oven at 70 °C overnight before use.

Synthesis of reduced NiFe-CPs (R-NiFe-CPs). To synthesize R-NiFe-CPs, the as-prepared NiFe-CP precursors (100 mg) were ultrasonically dispersed into 30 mL of ethanol for 15 min. Then, 60 mL of 0.3 M of sodium borohydride solution were rapidly injected into the above NiFe-CP dispersion. The mixed dispersion was stirred for 5 h at room temperature. The final precipitations (R-NiFe-CPs) were collected *via* centrifugation, washed with ethanol, and dried at 70 °C overnight.

Synthesis of S modified R-NiFe-CPs (S-R-NiFe-CPs). To prepare S-R-NiFe-CPs, a total of 20 mg of R-NiFe-CP precursors was ultrasonically dispersed into 6 mL of ethanol for 15 min. Meanwhile, a total of 2, 5, 10, 20, and 50 mg of thioacetamide was dissolved into 6 mL ethanol to form a transparent solution, respectively. The as-prepared thioacetamide solution was rapidly poured into the R-NiFe-CP dispersion and continuously stirred for 10 min. The dispersion mixture was then transferred into a Teflon-lined stainless steel autoclave (20 mL) and reacted at 120 °C, 140 °C, and 160 °C for 2 h, 4 h, and 6 h, respectively. The final precipitations (S-R-NiFe-CPs) were collected *via* centrifugation, washed with ethanol, and dried at 70 °C overnight. For comparison, R-NiFe-CPs without any sulfur modification (denoted as O_a-R-NiFe-CPs, O_a represents oxygen deficiencies) were also prepared through the same synthetic procedure in the absence of thioacetamide.

Synthesis of NiFe-based oxides (NiFe-O). NiFe-O were prepared by calcination of as-synthesized R-NiFe-CPs in air at 350 °C for 2 h.

Synthesis of S modified NiFe-based oxides (S-NiFe-O). S-NiFe-O were prepared via a similar synthetic strategy for S-R-NiFe-CPs, except for replacing R-NiFe-CPs precursors with the as-synthesized NiFe-O. For comparison, NiFe-based oxides were prepared via a similar hydrothermal reaction route without any thioacetamide additive. The as-obtained NiFe-based oxides obtained from the hydrothermal reaction were then denoted as NiFe-O.

ASSOCIATED CONTENT

Supporting Information

This material is available free of charge *via* the Internet at <http://pubs.acs.org>.

Details on the material characterizations (PXRD, FE-SEM, EDX, EPR, HR-STEM, XPS, and Raman), *operando* XAS measurements, electrochemical measurements (CV, C_{dl}, EIS, CA, RRDE, pH-dependent OER performance), and DFT calculations are provided in the Supporting Information, together with ICP-MS results, fitting parameters of XAS data, and surveys of OER activity.

AUTHOR INFORMATION

Corresponding Author

* E-mail: greta.patzke@chem.uzh.ch.

Author Contributions

Y. G. Zhao and W. C. Wan contributed equally. G. R. Patzke supervised this project. Y. G. Zhao and G. R. Patzke contributed to the original idea, experimental strategy, and manuscript writing. Y. G. Zhao performed all syntheses, characterizations, electrochemi-

cal performance tests, *operando* XAS tests, data analyses, and prepared the manuscript. W. C. Wan helped with data analyses and preparation of the manuscript. N. C. Dongfang and M. Iannuzzi performed the DFT calculations and data analysis. C. A. Triana and C. Huang helped with the XAS data analyses, conduction of *operando* XAS experiments, and data analysis. L. Douls performed parts of syntheses. R. Erni conducted HR-TEM and HAADF-STEM characterizations. All authors reviewed and commented on the manuscript before submission.

Notes

The authors declare no competing financial interest.

ACKNOWLEDGMENTS

Y. G. Zhao, W. C. Wan, N. C. Dongfang, C. A. Triana, L. Douls, C. Huang, M. Iannuzzi, and G. R. Patzke thank the University of Zurich Research Priority Program *Solar Light to Chemical Energy Conversion* (URPP LightChEC) for financial support. G. R. Patzke gratefully acknowledges financial support by the Swiss National Science Foundation (Sinergia Grant No. CRSI12_160801). The authors thank the Center for Microscopy and Image Analysis (UZH) for assistance and support in performing scanning electron microscopy experiments. We thank Viviane Grange (UZH) for ICP-MS measurements. We are grateful to ESRF-SNBL for the allocation of synchrotron radiation beamtime and to Dr. W. van Beek and Dr. D. Stoian for providing assistance in using the BM31 beamline and in setting up the *operando* XAS tests.

REFERENCES

- (1) Song, J.; Wei, C.; Huang, Z.-F.; Liu, C.; Zeng, L.; Wang, X.; Xu, Z. J. A Review on Fundamentals for Designing Oxygen Evolution Electrocatalysts. *Chem. Soc. Rev.* **2020**, *49*, 2196–2214.
- (2) Mefford, J. T.; Akbashev, A. R.; Kang, M.; Bentley, C. L.; Gent, W. E.; Deng, H. D.; Alsem, D. H.; Yu, Y.-S.; Salmon, N. J.; Shapiro, D. A.; Unwin, P. R.; Chueh, W. C. Correlative *Operando* Microscopy of Oxygen Evolution Electrocatalysts. *Nature* **2021**, *593*, 67–73.
- (3) Wang, H.; Zhuo, S.; Liang, Y.; Han, X.; Zhang, B. General Self-Template Synthesis of Transition-Metal Oxide and Chalcogenide Mesoporous Nanotubes with Enhanced Electrochemical Performances. *Angew. Chem. Int. Ed.* **2016**, *55*, 9055–9059.
- (4) Zhuo, S.; Shi, Y.; Liu, L.; Li, R.; Le Shi; Anjum, D. H.; Han, Y.; Wang, P. Dual-Template Engineering of Triple-Layered Nanoarray Electrode of Metal Chalcogenides Sandwiched with Hydrogen-Substituted Graphdiyne. *Nat. Commun.* **2018**, *9*, 3132.
- (5) Hausmann, J. N.; Schlögl, R.; Menezes, P. W.; Driess, M. Is Direct Seawater Splitting Economically Meaningful? *Energy Environ. Sci.* **2021**, *14*, 3679–3685.
- (6) Huang, Z.-F.; Song, J.; Dou, S.; Li, X.; Wang, J.; Wang, X. Strategies to Break the Scaling Relation Toward Enhanced Oxygen Electrocatalysis. *Matter* **2019**, *1*, 1494–1518.
- (7) Huang, Z.-F.; Song, J.; Du, Y.; Xi, S.; Dou, S.; Nsanzimana, J. M. V.; Wang, C.; Xu, Z. J.; Wang, X. Chemical and Structural Origin of Lattice Oxygen Oxidation in Co–Zn Oxyhydroxide Oxygen Evolution Electrocatalysts. *Nat. Energy* **2019**, *4*, 329–338.
- (8) Khani, H.; Grundish, N. S.; Wipf, D. O.; Goodenough, J. B. Graphitic-Shell Encapsulation of Metal Electrocatalysts for Oxygen Evolution, Oxygen Reduction, and Hydrogen Evolution in Alkaline Solution. *Adv. Energy Mater.* **2020**, *10*, 1903215.
- (9) Li, S.; Chen, B.; Wang, Y.; Ye, M.-Y.; van Aken, P. A.; Cheng, C.; Thomas, A. Oxygen-Evolving Catalytic Atoms on Metal Carbides. *Nat. Mater.* **2021**, *20*, 1240–1247.
- (10) Zhao, Y.; Wan, W.; Chen, Y.; Erni, R.; Triana, C. A.; Li, J.; Mavrokefalos, C. K.; Zhou, Y.; Patzke, G. R. Understanding and Optimizing Ultra-Thin Coordination Polymer Derivatives with High Oxygen Evolution Performance. *Adv. Energy Mater.* **2020**, *10*, 2002228.

- (11) Tian, T.; Zheng, M.; Lin, J.; Meng, X.; Ding, Y. Amorphous Ni-Fe Double Hydroxide Hollow Nanocubes Enriched with Oxygen Vacancies As Efficient Electrocatalytic Water Oxidation Catalysts. *Chem. Commun.* **2019**, *55*, 1044–1047.
- (12) Hu, C.; Hu, Y.; Fan, C.; Yang, L.; Zhang, Y.; Li, H.; Xie, W. Surface-Enhanced Raman Spectroscopic Evidence of Key Intermediate Species and Role of NiFe Dual-Catalytic Center in Water Oxidation. *Angew. Chem. Int. Ed.* **2021**, *60*, 19774–19778.
- (13) Cui, M.; Yang, C.; Li, B.; Dong, Q.; Wu, M.; Hwang, S.; Xie, H.; Wang, X.; Wang, G.; Hu, L. High-Entropy Metal Sulfide Nanoparticles Promise High-Performance Oxygen Evolution Reaction. *Adv. Energy Mater.* **2021**, *11*, 2002887.
- (14) Shi, Y.; Li, M.; Yu, Y.; Zhang, B. Recent Advances in Nanostructured Transition Metal Phosphides: Synthesis and Energy-Related Applications. *Energy Environ. Sci.* **2020**, *13*, 4564–4582.
- (15) Wu, Z.-P.; Zhang, H.; Zuo, S.; Wang, Y.; Zhang, S. L.; Zhang, J.; Zang, S.-Q.; Lou, X. W. Manipulating the Local Coordination and Electronic Structures for Efficient Electrocatalytic Oxygen Evolution. *Adv. Mater.* **2021**, *33*, 2103004.
- (16) Zhang, N.; Feng, X.; Rao, D.; Deng, X.; Cai, L.; Qiu, B.; Long, R.; Xiong, Y.; Lu, Y.; Chai, Y. Lattice Oxygen Activation Enabled by High-Valence Metal Sites for Enhanced Water Oxidation. *Nat. Commun.* **2020**, *11*, 4066.
- (17) Hu, C.; Hu, Y.; Fan, C.; Yang, L.; Zhang, Y.; Li, H.; Xie, W. Surface-Enhanced Raman Spectroscopic Evidence of Key Intermediate Species and Role of NiFe Dual-Catalytic Center in Water Oxidation. *Angew. Chem. Int. Ed.* **2021**, *60*, 19774–19778.
- (18) Wan, W.; Zhao, Y.; Wei, S.; Triana, C. A.; Li, J.; Arcifa, A.; Allen, C. S.; Cao, R.; Patzke, G. R. Mechanistic Insight into the Active Centers of Single/Dual-Atom Ni/Fe-Based Oxygen Electrocatalysts. *Nat. Commun.* **2021**, *12*, 5589.
- (19) Su, X.; Wang, Y.; Zhou, J.; Gu, S.; Li, J.; Zhang, S. *Operando* Spectroscopic Identification of Active Sites in NiFe Prussian Blue Analogues As Electrocatalysts: Activation of Oxygen Atoms for Oxygen Evolution Reaction. *J. Am. Chem. Soc.* **2018**, *140*, 11286–11292.
- (20) Lee, S.; Moysiadou, A.; Chu, Y.-C.; Chen, H. M.; Hu, X. Tracking High-Valent Surface Iron Species in the Oxygen Evolution Reaction on Cobalt Iron (Oxy)Hydroxides. *Energy Environ. Sci.* **2022**, *15*, 206–214.
- (21) Wei, C.; Rao, R. R.; Peng, J.; Huang, B.; Stephens, I. E. L.; Risch, M.; Xu, Z. J.; Shao-Horn, Y. Recommended Practices and Benchmark Activity for Hydrogen and Oxygen Electrocatalysis in Water Splitting and Fuel Cells. *Adv. Mater.* **2019**, *31*, 1806296.
- (22) Huang, Z.-F.; Xi, S.; Song, J.; Dou, S.; Li, X.; Du, Y.; Diao, C.; Xu, Z. J.; Wang, X. Tuning of Lattice Oxygen Reactivity and Scaling Relation to Construct Better Oxygen Evolution Electrocatalyst. *Nat. Commun.* **2021**, *12*, 3992.
- (23) Zhao, S.; Tan, C.; He, C.-T.; An, P.; Xie, F.; Jiang, S.; Zhu, Y.; Wu, K.-H.; Zhang, B.; Li, H.; Zhang, J.; Chen, Y.; Liu, S.; Dong, J.; Tang, Z. Structural Transformation of Highly Active Metal-Organic Framework Electrocatalysts During the Oxygen Evolution Reaction. *Nat. Energy* **2020**, *5*, 881–890.
- (24) Risch, M.; Ringleb, F.; Kohlhoff, M.; Bogdanoff, P.; Chernev, P.; Zaharieva, I.; Dau, H. Water Oxidation by Amorphous Cobalt-Based Oxides: *In Situ* Tracking of Redox Transitions and Mode of Catalysis. *Energy Environ. Sci.* **2015**, *8*, 661–674.
- (25) Triana, C. A.; Moré, R.; Bloomfield, A. J.; Petrović, P. V.; Ferrón, S. G.; Stanley, G.; Zarić, S. D.; Fox, T.; Brothers, E. N.; Sheehan, S. W.; Anastas, P. T.; Patzke, G. R. Soft Templating and Disorder in an Applied 1d Cobalt Coordination Polymer Electrocatalyst. *Matter* **2019**, *1*, 1354–1369.
- (26) Tian, T.; Gao, H.; Zhou, X.; Zheng, L.; Wu, J.; Li, K.; Ding, Y. Study of the Active Sites in Porous Nickel Oxide Nanosheets by Manganese Modulation for Enhanced Oxygen Evolution Catalysis. *ACS Energy Lett.* **2018**, *3*, 2150–2158.
- (27) Zhao, Y.; Mavrokefalos, C. K.; Zhang, P.; Erni, R.; Li, J.; Triana, C. A.; Patzke, G. R. Self-Templating Strategies for Transition Metal Sulfide Nanoboxes As Robust Bifunctional Electrocatalysts. *Chem. Mater.* **2020**, *32*, 1371–1383.
- (28) Görlin, M.; Chernev, P.; Ferreira de Araújo, J.; Reier, T.; Dresp, S.; Paul, B.; Krähnert, R.; Dau, H.; Strasser, P. Oxygen Evolution Reaction Dynamics, Faradaic Charge Efficiency, and the Active Metal Redox States of Ni-Fe Oxide Water Splitting Electrocatalysts. *J. Am. Chem. Soc.* **2016**, *138*, 5603–5614.
- (29) Bergmann, A.; Jones, T. E.; Martínez Moreno, E.; Teschner, D.; Chernev, P.; Gliech, M.; Reier, T.; Dau, H.; Strasser, P. Unified Structural Motifs of the Catalytically Active State of Co(Oxyhydr)Oxides During the Electrochemical Oxygen Evolution Reaction. *Nat. Catal.* **2018**, *1*, 711–719.
- (30) Wu, T.; Sun, S.; Song, J.; Xi, S.; Du, Y.; Chen, B.; Sasangka, W. A.; Liao, H.; Gan, C. L.; Scherer, G. G.; Zeng, L.; Wang, H.; Li, H.; Grimaud, A.; Xu, Z. J. Iron-Facilitated Dynamic Active-Site Generation on Spinel CoAl₂O₄ with Self-Termination of Surface Reconstruction for Water Oxidation. *Nat. Catal.* **2019**, *2*, 763–772.
- (31) Hausmann, J. N.; Mebs, S.; Laun, K.; Zebger, I.; Dau, H.; Menezes, P. W.; Driess, M. Understanding the Formation of Bulk- and Surface-Active Layered (Oxy)Hydroxides for Water Oxidation Starting from a Cobalt Selenite Precursor. *Energy Environ. Sci.* **2020**, *13*, 3607–3619.
- (32) Zhuang, L.; Jia, Y.; Liu, H.; Li, Z.; Li, M.; Zhang, L.; Wang, X.; Yang, D.; Zhu, Z.; Yao, X. Sulfur-Modified Oxygen Vacancies in Iron-Cobalt Oxide Nanosheets: Enabling Extremely High Activity of the Oxygen Evolution Reaction to Achieve the Industrial Water Splitting Benchmark. *Angew. Chem. Int. Ed.* **2020**, *59*, 14664–14670.
- (33) Xiao, Z.; Huang, Y.; Dong, C.-L.; Xie, C.; Liu, Z.; Du, S.; Chen, W.; Yan, D.; Li Tao, S.; Zhang, G.; Duan, H.; Wang, Y.; Zou, Y.; Chen, R.; Wang, S. *Operando* Identification of the Dynamic Behavior of Oxygen Vacancy-Rich Co₃O₄ for Oxygen Evolution Reaction. *J. Am. Chem. Soc.* **2020**, *142*, 12087–12095.
- (34) Wan, W.; Triana, C. A.; Lan, J.; Li, J.; Allen, C. S.; Zhao, Y.; Iannuzzi, M.; Patzke, G. R. Bifunctional Single Atom Electrocatalysts: Coordination–Performance Correlations and Reaction Pathways. *ACS Nano* **2020**, *14*, 13279–13293.
- (35) Yan, D.; Li, Y.; Huo, J.; Chen, R.; Dai, L.; Wang, S. Defect Chemistry of Nonprecious-Metal Electrocatalysts for Oxygen Reactions. *Adv. Mater.* **2017**, *29*, 1606459.
- (36) Trześniewski, B. J.; Diaz-Morales, O.; Vermaas, D. A.; Longo, A.; Bras, W.; Koper, M. T.; Smith, W. A. *In Situ* Observation of Active Oxygen Species in Fe-Containing Ni-Based Oxygen Evolution Catalysts: The Effect of pH on Electrochemical Activity. *J. Am. Chem. Soc.* **2015**, *137*, 15112–15121.
- (37) Friebe, D.; Louie, M. W.; Bajdich, M.; Sanwald, K. E.; Cai, Y.; Wise, A. M.; Cheng, M.-J.; Sokaras, D.; Weng, T.-C.; Alonso-Mori, R.; Davis, R. C.; Bargar, J. R.; Nørskov, J. K.; Nilsson, A.; Bell, A. T. Identification of Highly Active Fe Sites in (Ni, Fe)OOH for Electrocatalytic Water Splitting. *J. Am. Chem. Soc.* **2015**, *137*, 1305–1313.
- (38) Smith, R. D. L.; Pasquini, C.; Loos, S.; Chernev, P.; Klingan, K.; Kubella, P.; Mohammadi, M. R.; González-Flores, D.; Dau, H. Geometric Distortions in Nickel (Oxy)Hydroxide Electrocatalysts by Redox Inactive Iron Ions. *Energy Environ. Sci.* **2018**, *11*, 2476–2485.
- (39) Bediako, D. K.; Lassalle-Kaiser, B.; Surendranath, Y.; Yano, J.; Yachandra, V. K.; Nocera, D. G. Structure–Activity Correlations in a Nickel–Borate Oxygen Evolution Catalyst. *J. Am. Chem. Soc.* **2012**, *134*, 6801–6809.
- (40) Ren, X.; Wei, C.; Sun, Y.; Liu, X.; Meng, F.; Meng, X.; Sun, S.; Xi, S.; Du, Y.; Bi, Z.; Shang, G.; Fisher, A. C.; Gu, L.; Xu, Z. J. Constructing an Adaptive Heterojunction As a Highly Active Catalyst for the Oxygen Evolution Reaction. *Adv. Mater.* **2020**, *32*, 2001292.
- (41) Kang, J.; Qiu, X.; Hu, Q.; Zhong, J.; Gao, X.; Huang, R.; Wan, C.; Liu, L.-M.; Duan, X.; Guo, L. Valence Oscillation and Dynamic Active Sites in Monolayer NiCo Hydroxides for Water Oxidation. *Nat. Catal.* **2021**, *4*, 1050–1058.
- (42) Görlin, M.; Ferreira de Araújo, J.; Schmies, H.; Bernsmeier, D.; Dresp, S.; Gliech, M.; Jusys, Z.; Chernev, P.; Kraehnert, R.; Dau, H.; Strasser, P. Tracking Catalyst Redox States and Reaction Dynamics in Ni-Fe Oxyhydroxide Oxygen Evolution Reaction Electrocatalysts: The Role of Catalyst Support and Electrolyte pH. *J. Am. Chem. Soc.* **2017**, *139*, 2070–2082.

- (43) Dionigi, F.; Zeng, Z.; Sinev, I.; Merzdorf, T.; Deshpande, S.; Lopez, M. B.; Kunze, S.; Zegkinoglou, I.; Sarodnik, H.; Fan, D.; Bergmann, A.; Drnec, J.; Araujo, J. F. de; Gliech, M.; Teschner, D.; Zhu, J.; Li, W.-X.; Greeley, J.; Cuenya, B. R.; Strasser, P. *In-Situ* Structure and Catalytic Mechanism of NiFe and CoFe Layered Double Hydroxides During Oxygen Evolution. *Nat. Commun.* **2020**, *11*, 2522.
- (44) Kim, B.-J.; Fabbri, E.; Abbott, D. F.; Cheng, X.; Clark, A. H.; Nachttegaal, M.; Borlaf, M.; Castelli, I. E.; Graule, T.; Schmidt, T. J. Functional Role of Fe-Doping in Co-Based Perovskite Oxide Catalysts for Oxygen Evolution Reaction. *J. Am. Chem. Soc.* **2019**, *141*, 5231–5240.
- (45) Li, N.; Bediako, D. K.; Hadt, R. G.; Hayes, D.; Kempa, T. J.; Cube, F. von; Bell, D. C.; Chen, L. X.; Nocera, D. G. Influence of Iron Doping on Tetravalent Nickel Content in Catalytic Oxygen Evolving Films. *PNAS* **2017**, *114*, 1486.
- (46) Zheng, X.; Zhang, B.; Luna, P. de; Liang, Y.; Comin, R.; Voznyy, O.; Han, L.; García de Arquer, F. Pelayo; Liu, M.; Dinh, C. T.; Regier, T.; Dynes, J. J.; He, S.; Xin, H. L.; Peng, H.; Prendergast, D.; Du, X.; Sargent, E. H. Theory-Driven Design of High-Valence Metal Sites for Water Oxidation Confirmed Using *In Situ* Soft X-Ray Absorption. *Nat. Chem.* **2018**, *10*, 149–154.
- (47) Görlin, M.; Halldin Stenlid, J.; Koroidov, S.; Wang, H.-Y.; Börner, M.; Shipilin, M.; Kalinko, A.; Murzin, V.; Safonova, O. V.; Nachttegaal, M.; Uheida, A.; Dutta, J.; Bauer, M.; Nilsson, A.; Diaz-Morales, O. Key Activity Descriptors of Nickel-Iron Oxygen Evolution Electrocatalysts in the Presence of Alkali Metal Cations. *Nat. Commun.* **2020**, *11*, 6181.
- (48) Bo, X.; Hocking, R. K.; Zhou, S.; Li, Y.; Chen, X.; Zhuang, J.; Du, Y.; Zhao, C. Capturing the Active Sites of Multimetallic (Oxy)Hydroxides for the Oxygen Evolution Reaction. *Energy Environ. Sci.* **2020**, *13*, 4225–4237.
- (49) Hao, Y.; Li, Y.; Wu, J.; Meng, L.; Wang, J.; Jia, C.; Liu, T.; Yang, X.; Liu, Z.-P.; Gong, M. Recognition of Surface Oxygen Intermediates on NiFe Oxyhydroxide Oxygen-Evolving Catalysts by Homogeneous Oxidation Reactivity. *J. Am. Chem. Soc.* **2021**, *143*, 1493–1502.
- (50) Radinger, H.; Connor, P.; Tengeler, S.; Stark, R. W.; Jaegermann, W.; Kaiser, B. Importance of Nickel Oxide Lattice Defects for Efficient Oxygen Evolution Reaction. *Chem. Mater.* **2021**, *33*, 8259–8266.
- (51) Li, J.; Wan, W.; Triana, C. A.; Chen, H.; Zhao, Y.; Mavrokefalos, C. K.; Patzke, G. R. Reaction Kinetics and Interplay of Two Different Surface States on Hematite Photoanodes for Water Oxidation. *Nat. Commun.* **2021**, *12*, 255.
- (52) Kuai, C.; Zhang, Y.; Wu, D.; Sokaras, D.; Mu, L.; Spence, S.; Nordlund, D.; Lin, F.; Du, X.-W. Fully Oxidized Ni–Fe Layered Double Hydroxide with 100% Exposed Active Sites for Catalyzing Oxygen Evolution Reaction. *ACS Catal.* **2019**, *9*, 6027–6032.
- (53) Zhao, Y.; Dongfang, N.; Triana, C.; A. Huang, C.; Emi, R.; Wan, W.; Li, J.; Stoian, D.; Pan, L.; Zhang, P.; Lan, J.; Iannuzzi M.; Patzke, G. R. Dynamics and Control of Active Sites in Hierarchically Nanostructured Cobalt Phosphide/Chalcogenide-Based Electrocatalysts for Water Splitting. *Energy Environ. Sci.*, **2022**, *15*, 727–739.
- (54) Chen, J. Y. C.; Dang, L.; Liang, H.; Bi, W.; Gerken, J. B.; Jin, S.; Alp, E. E.; Stahl, S. S. *Operando* Analysis of NiFe and Fe Oxyhydroxide Electrocatalysts for Water Oxidation: Detection of Fe⁴⁺ by Mössbauer Spectroscopy. *J. Am. Chem. Soc.* **2015**, *137*, 15090–15093.
- (55) Zhu, K.; Zhu, X.; Yang, W. Application of *In Situ* Techniques for the Characterization of NiFe-Based Oxygen Evolution Reaction (OER) Electrocatalysts. *Angew. Chem. Int. Ed.* **2019**, *58*, 1252–1265.
- (56) Grimaud, A.; Diaz-Morales, O.; Han, B.; Hong, W. T.; Lee, Y.-L.; Giordano, L.; Stoerzinger, K. A.; Koper, M. T. M.; Shao-Horn, Y. Activating Lattice Oxygen Redox Reactions in Metal Oxides to Catalyze Oxygen Evolution. *Nat. Chem.* **2017**, *9*, 457–465.
- (57) Bai, L.; Lee, S.; Hu, X. Spectroscopic and Electrokinetic Evidence for a Bifunctional Mechanism of the Oxygen Evolution Reaction. *Angew. Chem. Int. Ed.* **2021**, *60*, 3095–3103.
- (58) Wang, H.; Wu, J.; Dolocan, A.; Li, Y.; Lü, X.; Wu, N.; Park, K.; Xin, S.; Lei, M.; Yang, W.; Goodenough, J. B. Short O–O Separation in Na_{0.67}CoO₂ Layered Oxide Enables an Ultrafast Oxygen Evolution Reaction. *PNAS* **2019**, *116*, 23473.
- (59) Pan, Y.; Xu, X.; Zhong, Y.; Ge, L.; Chen, Y.; Veder, J.-P. M.; Guan, D.; O’Hayre, R.; Li, M.; Wang, G.; Wang, H.; Zhou, W.; Shao, Z. Direct Evidence of Boosted Oxygen Evolution Over Perovskite by Enhanced Lattice Oxygen Participation. *Nat. Commun.* **2020**, *11*, 2002.
- (60) Grimaud, A.; Hong, W. T.; Shao-Horn, Y.; Tarascon, J.-M. Anionic Redox Processes for Electrochemical Devices. *Nat. Mater.* **2016**, *15*, 121–126.
- (61) Hong, W. T.; Stoerzinger, K. A.; Lee, Y.-L.; Giordano, L.; Grimaud, A.; Johnson, A. M.; Hwang, J.; Crumlin, E. J.; Yang, W.; Shao-Horn, Y. Charge-Transfer-Energy-Dependent Oxygen Evolution Reaction Mechanisms for Perovskite Oxides. *Energy Environ. Sci.* **2017**, *10*, 2190–2200.